

Article

# The Influence of Zn Substitution on Physical Properties of $\text{CoFe}_2\text{O}_4$ Nanoparticles

Adam Szatmari<sup>1</sup>, Rares Bortnic<sup>1</sup>, Gabriela Souca<sup>1</sup>, Razvan Hirian<sup>1</sup>, Lucian Barbu-Tudoran<sup>2,3</sup>, Fran Nekvapil<sup>1,4</sup>, Cristian Iacovita<sup>5</sup>, Emil Burzo<sup>1</sup>, Roxana Dudric<sup>1,\*</sup> and Romulus Tetean<sup>1,\*</sup>

<sup>1</sup> Faculty of Physics, “Babes Bolyai” University, Kogalniceanu 1, 400084 Cluj-Napoca, Romania

<sup>2</sup> Electron Microscopy Center “Prof. C. Craciun”, Faculty of Biology & Geology, “Babes-Bolyai” University, 5-7 Clinicilor St., 400006 Cluj-Napoca, Romania

<sup>3</sup> Integrated Electron Microscopy Laboratory, National Institute for Research and Development of Isotopic and Molecular Technologies, 67-103 Donat St., 400293 Cluj-Napoca, Romania

<sup>4</sup> RDI Laboratory of Applied Raman Spectroscopy, RDI Institute of Applied Natural Sciences (IRDI-ANS), Babeş-Bolyai University, Fântânele 42, 400293 Cluj-Napoca, Romania

<sup>5</sup> Department of Pharmaceutical Physics-Biophysics, Faculty of Pharmacy, Iuliu Hatieganu University of Medicine and Pharmacy, 6 Pasteur St., 400349 Cluj-Napoca, Romania

\* Correspondence: roxana.dudric@ubbcluj.ro (R.D.); romulus.tetean@ubbcluj.ro (R.T.); Tel.: +40-741033325 (R.T.)

**Abstract:**  $\text{Co}_{1-x}\text{Zn}_x\text{Fe}_2\text{O}_4$  nanoparticles ( $0 \leq x \leq 1$ ) have been synthesized via a green sol-gel combustion method. The prepared samples were studied using X-ray diffraction measurements (XRD), transmission electron microscopy (TEM), Raman, and magnetic measurements. All samples were found to be single phases and have a cubic  $Fd-3m$  structure. EDS analysis confirmed the presence of cobalt, zinc, iron, and oxygen in all studied samples. Raman spectra clearly show that Zn ions are preferentially located in T sites for low Zn concentrations. Due to their high crystallinity, the nanoparticles show high values of the magnetization, which increases with the Zn content for  $x < 0.5$ . The magnetic properties are discussed based on Raman results. Co ferrite doped with 30% of Zn produced the largest SAR values, which increase linearly from 148 to 840 W/g<sub>MNPs</sub> as the H is increased from 20 to 60 kA/m.

**Keywords:** zinc-cobalt ferrite nanoparticles; Raman measurements; magnetic properties



**Citation:** Szatmari, A.; Bortnic, R.; Souca, G.; Hirian, R.; Barbu-Tudoran, L.; Nekvapil, F.; Iacovita, C.; Burzo, E.; Dudric, R.; Tetean, R. The Influence of Zn Substitution on Physical Properties of  $\text{CoFe}_2\text{O}_4$  Nanoparticles. *Nanomaterials* **2023**, *13*, 189. <https://doi.org/10.3390/nano13010189>

Academic Editors: Fabien Grasset and Julian Maria Gonzalez Estevez

Received: 28 November 2022

Revised: 23 December 2022

Accepted: 27 December 2022

Published: 31 December 2022



**Copyright:** © 2022 by the authors. Licensee MDPI, Basel, Switzerland. This article is an open access article distributed under the terms and conditions of the Creative Commons Attribution (CC BY) license (<https://creativecommons.org/licenses/by/4.0/>).

## 1. Introduction

Magnetic materials with nanometer crystalline sizes are the focus of a large number of researchers due to their interesting changes on physical properties compared to that of their bulk correspondent. The physical properties of these materials can be easily tuned and depend strongly on the chemical composition, crystal structure, shape, and size of the nanoparticle, as well as the cation distribution [1,2]. Among these, cobalt ferrite with or without substitution on cobalt site is technologically important for applications in different fields: biomedicine, anti-cancer drugs, cellular therapy, active components in ferrofluids, magnetic refrigeration, information and energy storage media, sensors, switching devices, high frequency electric devices, recording heads, catalysis, magnetic cell separation, hyperthermia, antibacterial agents, permanent magnets, medical imaging, etc. [3–15].

$\text{CoFe}_2\text{O}_4$  presents high coercivity, high cubic magneto crystalline anisotropy, moderate saturation magnetization, large magnetostrictive coefficient, and low toxicity [16–21]. On the other hand, cobalt ferrite exhibit high mechanical stiffness and chemical stability.

The  $\text{CoFe}_2\text{O}_4$ , or  $(\text{Co}_{1-x}\text{Fe}_x)_\text{T}(\text{Co}_x\text{Fe}_{2-x})_\text{O}_4$  structure, where  $x$  is the inversion parameter, presents a variable occupancy of tetrahedral (T) and octahedral sites (O). The structure changes from a normal spinel ( $x = 0$ ) to an inverse spinel type ( $x = 1$ ). In bulk

state, the  $\text{CoFe}_2\text{O}_4$  ferrite has a predominantly inverse-type spinel structure and crystallizes in a fcc-type lattice, space group  $Fm\bar{3}m$ .  $\text{CoFe}_2\text{O}_4$  is ferrimagnetically ordered, with the magnetic moments of the atoms situated in T and O sublattices being antiparallely aligned. Depending on the preparation method and the annealing temperature,  $\text{Co}^{2+}$  ions could reside in octahedral sites and will strongly influence the structural, magnetic, and electric properties [22–24].

$\text{ZnFe}_2\text{O}_4$  crystallize in a normal spinel structure with the  $\text{Zn}^{2+}$  ions located mainly in the T sites and  $\text{Fe}^{3+}$  ions located in O sites [16,25]. It was reported that the cobalt ferrite physical properties can be adjusted by the substitution with magnetic or non-magnetic ions. Li et al. have reported that the saturation magnetization of  $\text{Co}_{1-x}\text{Zn}_x\text{Fe}_2\text{O}_4$  (prepared using the sol–gel method) increase when Zn ions concentration increases up to  $x = 0.4$ , followed by a large decrease for  $x > 0.5$  [26]. The initial increase in the magnetization was explained by the preferential occupation of T sites by  $\text{Zn}^{2+}$ . When the zinc concentration increases more, the exchange interactions between  $\text{Fe}^{3+}$  ions decrease due to the lack of magnetic neighbors and the saturation magnetization decreases. Later, Slatineanu et al. reported that on the same system, prepared by chemical co-precipitation method, the compound with  $x = 0.2$  is optimum considering magnetic and dielectric properties [27]. Atif et al. has shown that the maximum value of the saturation magnetization on  $\text{Co}_{1-x}\text{Zn}_x\text{Fe}_2\text{O}_4$  prepared by sol–gel method was obtained for  $x = 0.4$  and was explained by the preferential occupation of T sites by Zn ions [28]. Tanaka et al. have prepared zinc ferrites by precipitation of the rapidly quenched oxides [29]. Small amounts of Zn and magnetite was found in the prepared samples. From Zn K-edge EXAFS studies, it was shown that some of the  $\text{Zn}^{2+}$  ions occupy octahedral sites together with the occupancy of tetrahedral sites by the  $\text{Fe}^{3+}$  ions.

Previously, we have studied the structural and magnetic properties of  $\text{CoFe}_2\text{O}_4$  nanoparticles and  $\text{CoFe}_2\text{O}_4 @\text{SiO}_2 @\text{Au}$  nanocomposites designed for magnetoplasmonic applications [30,31]. To check the Zn ion occupancy in the cobalt ferrite structure and to improve the values of saturation magnetization, we have prepared cobalt ferrites with Zn substitution at Co sites in very large concentration ranges. In this paper, we present our results on the influence of Zn on the structural and physical properties of cobalt ferrite. The  $\text{Co}_{1-x}\text{Zn}_x\text{Fe}_2\text{O}_4$  nanoparticles have been synthesized via a green sol–gel combustion method. Chemical reduction, often used to produce nanoferrites, utilizes organic solvents. Risk-free chemicals, environmentally mild solvents and feasible materials are key factors to the application of green strategies [32,33]. The green synthesis of nanoparticles denotes a development above other methods, since it is simpler, easy to use, and the obtained nanoferrites are often more stable. The prepared samples were studied using X-ray diffraction measurements (XRD), transmission electron microscopy (TEM), scanning electron microscopy (SEM), Raman, and magnetic measurements. Raman spectra clearly show that Zn ions are preferentially located in T sites for low Zn concentrations. The magnetic properties are discussed based on Raman results.

## 2. Materials and Methods

### 2.1. Samples Preparation

$\text{Co}_{1-x}\text{Zn}_x\text{Fe}_2\text{O}_4$  ( $x = 0, 0.05, 0.1, 0.2, 0.3, 0.4, 0.5, 0.6, 0.7, 0.8, 0.9, 1$ ) nanoparticles were synthesized via a green, sucrose, and pectin-based, sol–gel combustion method. The synthesis can be considered green as both the poly-condensation and chelating agents were molecules of vegetal origin. The sucrose used was extracted from sugar beets and the pectin used for the synthesis was extracted from citrus fruits. The reagents,  $\text{Fe}(\text{NO}_3)_3 \cdot 9\text{H}_2\text{O}$  (Iron(III) nitrate nonahydrate),  $\text{Co}(\text{NO}_3)_2 \cdot 6\text{H}_2\text{O}$  (Cobalt nitrate hexahydrate 97.7%),  $\text{Zn}(\text{NO}_3)_2$  (Zinc nitrate hexahydrate 98%), were purchased from Alfa Aesar. All calculations were performed for 2 mmols of nanoparticles. Stoichiometric quantities of each precursor were weighed and dissolved in Milli-Q water under vigorous magnetic stirring at 60 °C. After 1 h, 14.9 mmols sucrose ( $\approx 5$  g) was added to each solution. After the full homogenization, the pH of the solutions was lowered to approximately 2 using a 65%  $\text{HNO}_3$  solution. For each solution, one gram of pectin was weighed and slowly added

to the mixture under magnetic stirring. This was performed in order to stop the pectin from agglomerating. After 20 more minutes of further stirring, the solutions were poured in ceramic capsules and placed on a sand bath at 240 °C for 24 h in order to evaporate the water and obtain the gel. The spongy, dried gel was then annealed in air at 700 °C for 2 h in order to decompose the organic part of the gel. A fine nanopowder was obtained.

## 2.2. Characterization

The crystal structure and crystallite sizes of  $\text{Co}_{1-x}\text{Zn}_x\text{Fe}_2\text{O}_4$  nanoparticles were determined by XRD measurements, performed at ambient temperature, with a Bruker D8 Advance diffractometer. The intensities were measured from 20° to 80° in continuous mode with a step size of 0.03° and a counting rate of 5 s per scanning step. The lattice parameters were obtained by Rietveld refinement of XRD patterns using FullProf Suite Software [34]. The instrumental resolution function (IRF) was evaluated by fitting the diffraction pattern of an LaB6 NIST standard and recorded under the same experimental conditions as those used for measuring the ferrite nanoparticles, and the IRF data file was provided to the program in order to allow subsequent refinement of the diffraction pattern of the samples. The refinement was performed based on the Thompson–Cox–Hastings pseudo-Voigt functions for peaks profile and the refined parameters were the lattice parameter, oxygen position, zero-shift correction, background parameters, isotropic temperature factor, and peak shape parameters. The crystallite sizes were estimated using the Debye–Scherrer equation:

$$D = \frac{k\lambda}{\beta \cos \theta} \quad (1)$$

where  $\beta$  is the peak full width at half maximum (in radians) at the observed peak angle  $\theta$ ,  $k$  is the crystallite shape factor (was considered 0.9), and  $\lambda$  is the X-ray wavelength.

The morphology of the synthesized nanoparticles was investigated by transmission electron microscopy (TEM) and scanning electron microscopy (SEM) using a Hitachi HD2700 CFEG STEM at 200 kV with secondary electron imaging capability. The energy dispersive X-ray spectroscopy (EDS) measurements were performed in order to analyze the composition of the prepared nanocomposites.

Dry nanoparticles were resuspended in 0.5 mL of distilled water and sonicated for 10 s in an ultrasonic bath to obtain a suspension. From here, 10  $\mu\text{L}$  were pipetted onto a quartz plate enabling firm and localized adhesion of the nanoparticles. Micro-Raman analysis was done after complete water evaporation. A Renishaw InVia Reflex confocal Raman microscope was used for structural analysis, using 100 $\times$  objective (NA 0.9) and He-Ne laser emitting at 632.8 nm (full power 17 mW). The spectra were acquired from the nanoparticle aggregates about 5  $\mu\text{m}$  large, with 60 s integration, 5 additive scans per spectrum, and 1.7 mW laser power. These conditions allowed the acquisition of Raman signal of sufficient intensity without causing phase transitions or fluorescence from the sample due to laser heat input [35]. At least 3 spectra were acquired from different points of each sample. Raman spectra were processed in Origin 8.5 software.

Magnetic measurements were performed in the 4.2–300 K temperature range and external magnetic fields up to 10 T by using a vibrating sample magnetometer from Cryogenic Limited London. The heating efficiency was evaluated using a commercially available magnetic hyperthermia system, the Easy Heat 0224 from Ambrell (Scottsville, NY, USA), equipped with an optical fiber temperature sensor (0.1 °C accuracy), providing alternating magnetic field (AMF) of fixed frequency (355 kHz) and variable amplitude (5–65 kA/m). Details about specific absorption rate (SAR) calculations are provided in the Supplementary Materials (Section S1).

## 3. Results

### 3.1. Morphology and Crystal Structure

The X-ray diffraction (XRD) measurements (Figure 1a) indicate that all samples are single phases and have a cubic  $Fd-3m$  structure. In order to determine the lattice parameters,

Rietveld analysis was performed for all samples using FullProf software [34], as shown for  $\text{Co}_{0.7}\text{Zn}_{0.3}\text{Fe}_2\text{O}_4$  in Figure 1b. The Rietveld analysis shows an almost linear increase in the lattice parameter/unit cell volume with the Zn content (Table 1), as expected considering the larger ionic radius of Zn, as compared with that of Co ions. The lattice parameter values and their Zn content dependence is close to that previously reported by other groups in a narrower concentration range [27–29] and opposite to ref. [26], where a decrease was shown with a minimum at  $x = 0.3$  followed by a nonlinear increase with Zn content. The crystallinity of our samples is probably higher than in that case.

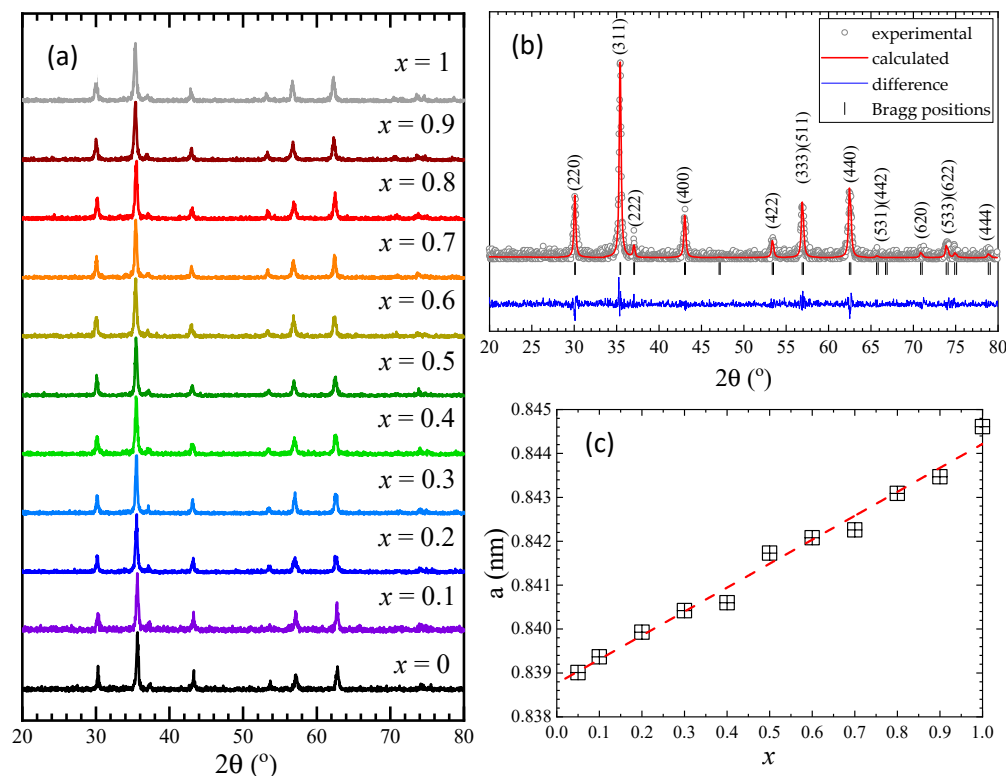


**Figure 1.** (a) XRD patterns at room temperature of  $\text{Co}_{1-x}\text{Zn}_x\text{Fe}_2\text{O}_4$  nanoparticles, (b) Rietveld refinement results for  $\text{Co}_{0.7}\text{Zn}_{0.3}\text{Fe}_2\text{O}_4$ , (c) The lattice parameter/unit cell volume dependence with Zn concentration for  $\text{Co}_{1-x}\text{Zn}_x\text{Fe}_2\text{O}_4$ .

**Table 1.** Structural parameters and Rietveld agreement factors, such as weighted profile factor ( $R_{wp}$ ), expected factor ( $R_{exp}$ ), and goodness-of-fit ( $\chi^2$ ), of  $\text{Co}_{1-x}\text{Zn}_x\text{Fe}_2\text{O}_4$  nanoparticles.

$x$	Lattice Parameter $a$ (nm)	$\chi^2$	$R_{wp}$	$R_{exp}$
0.05	0.8390 (1)	1.04	7.08	6.95
0.1	0.8393 (7)	1.03	7.27	7.15
0.2	0.8399 (2)	0.934	5.90	6.11
0.3	0.8404 (1)	0.937	5.71	5.91
0.4	0.8405 (5)	0.994	5.95	5.97
0.5	0.8418 (0)	0.948	5.56	5.72
0.6	0.8421 (0)	1.00	5.65	5.64
0.7	0.8422 (4)	1.03	5.47	5.39
0.8	0.8430 (9)	0.988	5.75	5.79
0.9	0.8434 (7)	0.970	5.34	5.42
1	0.8446 (1)	0.975	5.53	5.60

The crystallite sizes, calculated using the Debye–Scherrer formula after subtracting the instrumental peak broadening, were found to be between 30 nm and 40 nm for all investigated  $\text{Co}_{1-x}\text{Zn}_x\text{Fe}_2\text{O}_4$  samples.

The TEM investigations of the  $\text{Co}_{1-x}\text{Zn}_x\text{Fe}_2\text{O}_4$  samples reveal that well-defined nanoparticles tend to agglomerate due to their significant magnetic interaction that competes with the much weaker electrostatic repulsion (Figure 2). The analysis of the TEM images shows the presence of nanoparticles of sizes between 15 nm and 70 nm, with a mean diameter close to the values obtained from XRD (Table 2), indicating that most of the  $\text{Co}_{1-x}\text{Zn}_x\text{Fe}_2\text{O}_4$  nanoparticles are single crystals and have high crystallinity. One can see that the nanoparticles are highly polydisperse and the error bars of the dimensions obtained from TEM measurements indicate that the nanoparticles' average diameters could be higher compared with the mean diameter obtained from XRD data.

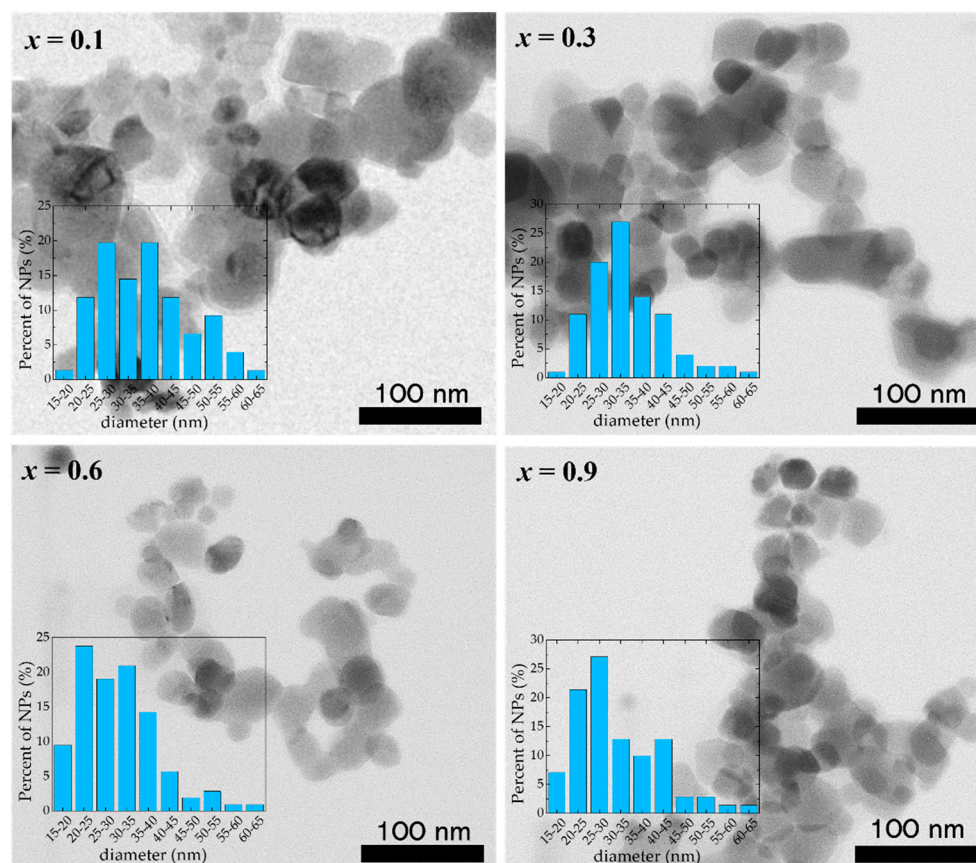


**Figure 2.** TEM images of  $\text{Co}_{1-x}\text{Zn}_x\text{Fe}_2\text{O}_4$  nanoparticles.

**Table 2.** Average  $\text{Co}_{1-x}\text{Zn}_x\text{Fe}_2\text{O}_4$  nanoparticles' size determined from XRD and TEM investigations, and atomic elemental composition theoretically calculated and determined from EDS measurements.

$x$	Mean Diameter (nm)		Atomic Abundance (Atoms %)							
	XRD	TEM	Co th.	Co exp.	Zn th.	Zn e.	Fe th.	Fe exp.	O th.	O exp.
0.1	$35 \pm 2$	$38 \pm 11$	12.8	11.5	1.4	1.1	28.5	21.3	57.3	66.1
0.3	$36 \pm 2$	$35 \pm 9$	10.0	9.0	4.2	1.6	28.5	21.4	57.3	68.0
0.6	$31 \pm 1$	$31 \pm 10$	5.7	5.9	8.5	5.2	28.5	22.9	57.3	66.0
0.9	$32 \pm 1$	$31 \pm 10$	1.4	1.9	12.8	9.0	28.5	23.6	57.3	65.5

Elemental analysis by EDS confirmed the presence of Co, Fe, Zn, and O elements in all studied samples. An example of the EDS spectra for  $\text{Co}_{0.4}\text{Zn}_{0.6}\text{Fe}_2\text{O}_4$  nanoparticles is given in Figure 3. The EDS spectra indicate that there are no other impurities present in the nanoparticles. The elemental mapping for the sample with  $x = 0.6$  is shown in Figure 4. One can see that the Co, Zn, Fe, and O elements are almost homogeneously distributed across the selected zone of the samples investigated. Similar results were obtained for all

studied samples. The elemental abundances for the studied samples are listed in Table 2. These data show that the concentrations of Zn, Co, and Fe elements in the resulting product are in a close agreement with the expected stoichiometric ratio.

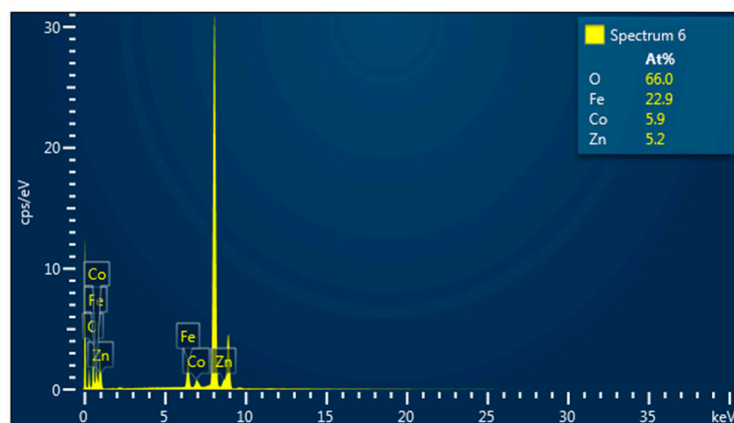


Figure 3. EDS spectra for  $\text{Co}_{0.4}\text{Zn}_{0.6}\text{Fe}_2\text{O}_4$  nanoparticles.

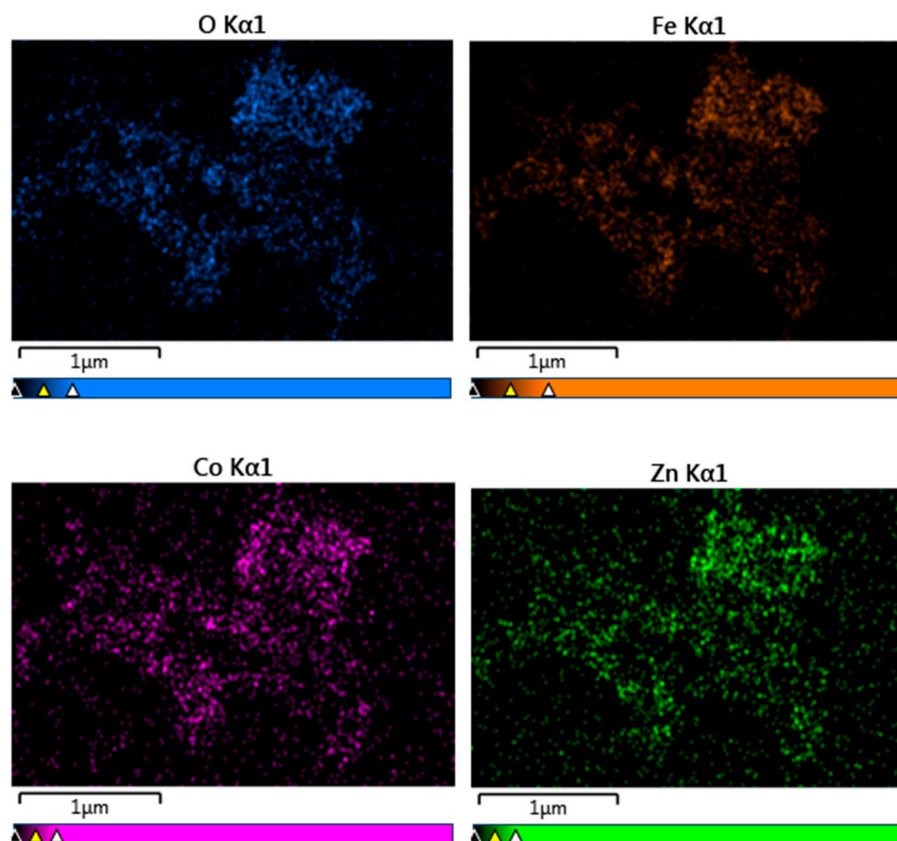


Figure 4. Elemental mapping of  $\text{Co}_{0.4}\text{Zn}_{0.6}\text{Fe}_2\text{O}_4$  nanoparticles.

### 3.2. Raman Spectra

Raman spectroscopy is a useful tool in analyzing the cation distribution in spinels. The cubic inverse/mixed ferrite structure gives rise to 39 normal vibrational modes, out of which 5 are Raman active:  $A_{1g}$ ,  $E_g$ , and  $3T_{2g}$  [36–39]. The Raman band configuration of iron oxides [35], face-centered cubic structure ferrites with  $Fd-3m$  symmetry, such as magnetite and maghemite [40] and doped ferrites [41–45], has been explored by several previous studies. Above  $600\text{ cm}^{-1}$ , the observed  $A_{1g}$  Raman modes are due to the symmetric metal-

O stretching vibrations at tetrahedral sites, while the lower  $T_{2g}$  and  $E_g$  frequency modes are associated with metal-O vibrations at octahedral sites [46].

Figure 5 shows the Raman spectra recorded for  $Co_{1-x}Zn_xFe_2O_4$  nanoparticles as  $0.05 \leq x \leq 0.9$ . The  $T_{2g}(1)$  band is centered at about  $180\text{ cm}^{-1}$ , slightly lower than observed in magnetite ( $196\text{ cm}^{-1}$ ) and higher than in Mn-Zn-doped ferrites ( $170\text{ cm}^{-1}$ ) [44]. Above  $200\text{ cm}^{-1}$ , the Raman spectra of  $Co_{1-x}Zn_xFe_2O_4$  nanoparticles show several modes, located at about  $310\text{ cm}^{-1}$ ,  $350\text{ cm}^{-1}$ ,  $470\text{ cm}^{-1}$ ,  $560\text{ cm}^{-1}$ ,  $610\text{ cm}^{-1}$ ,  $650\text{ cm}^{-1}$ , and  $690\text{ cm}^{-1}$ , that change in intensity with the Zn content. In order to assign the different contributions to the recorded spectra, the modes associated with Co, Zn, and Fe ions located in the tetrahedral and/or octahedral sites have been considered. In cobalt ferrite, the  $A_{1g}$  modes located at about  $620\text{ cm}^{-1}$  and  $695\text{ cm}^{-1}$  were found to correspond to Co and Fe ions located at the tetrahedral site, while the  $T_{2g}(3)$  modes, corresponding to the Fe and Co ions at the octahedral sites, are located at about  $470\text{ cm}^{-1}$  and  $575\text{ cm}^{-1}$  [41]. A detailed analysis of the Raman spectra in  $ZnFe_2O_4$  revealed that the  $A_{1g}$  broad peak around  $650\text{ cm}^{-1}$  is the result of the overlapping of two signals centered around  $641\text{ cm}^{-1}$  and  $685\text{ cm}^{-1}$ , which correspond to the modes inside  $ZnO_4$  and  $FeO_4$  units, while the  $T_{2g}(3)$  modes due to the Fe and Zn ions are located at about  $470\text{ cm}^{-1}$  and  $510\text{ cm}^{-1}$  [46].

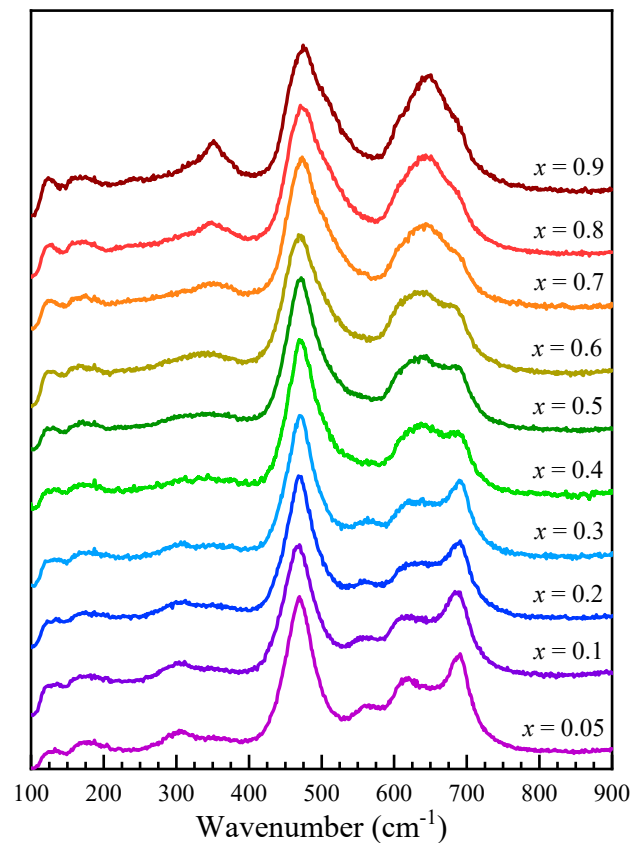


**Figure 5.** Raman spectra of  $Co_{1-x}Zn_xFe_2O_4$  nanoparticles.

Raman spectroscopy analysis and spectra deconvolution was conducted primarily to explore if cation distribution between the tetrahedral and octahedral sites can be quantified. The movement of additional cation types to tetrahedral sites adds new components to the  $A_{1g}$  band, the position of which is loosely correlated to respective ionic radius of the dopant [44]. Tetrahedrally coordinated zinc within ferrites exhibits a band in the  $630\text{--}650\text{ cm}^{-1}$  range [44–46], well separated from the Co–O and Fe–O bands. Indeed, the fits show the three  $A_{1g}$  components at  $605\text{--}610\text{ cm}^{-1}$  representing Co–O, at  $635\text{--}650\text{ cm}^{-1}$  representing Zn–O, and at  $680\text{--}690\text{ cm}^{-1}$  representing Fe–O vibrations.

In order to analyze the cation distribution, the Raman spectra of  $\text{Co}_{1-x}\text{Zn}_x\text{Fe}_2\text{O}_4$  nanoparticles were fitted with six components in the region between  $380\text{ cm}^{-1}$  and  $800\text{ cm}^{-1}$ , which correspond to the Fe, Zn, and Co ions located in the tetrahedral and octahedral sites, with widths between  $40\text{ cm}^{-1}$  and  $70\text{ cm}^{-1}$ . The fitting results indicate position shifts with only up to  $\pm 10\text{ cm}^{-1}$ , indicating the preservation of the general Co ferrite phase (Table 3).

**Table 3.** Fitting results of the main Raman modes for  $\text{Co}_{1-x}\text{Zn}_x\text{Fe}_2\text{O}_4$  nanoparticles.

$x$	$T_{2g}$		$A_{1g}$	
	Energy ( $\text{cm}^{-1}$ )	FWHM ( $\text{cm}^{-1}$ )	Energy ( $\text{cm}^{-1}$ )	FWHM ( $\text{cm}^{-1}$ )
0.05	$467 \pm 1$ (Fe–O)	$57 \pm 5$	$610 \pm 1$ (Co–O)	$54 \pm 5$
	$510 \pm 1$ (Zn–O)	$43 \pm 5$	$647 \pm 1$ (Zn–O)	$46 \pm 5$
	$557 \pm 1$ (Co–O)	$62 \pm 5$	$686 \pm 1$ (Fe–O)	$47 \pm 5$
0.1	$465 \pm 1$ (Fe–O)	$56 \pm 5$	$604 \pm 1$ (Co–O)	$54 \pm 5$
	$506 \pm 1$ (Zn–O)	$42 \pm 5$	$641 \pm 1$ (Zn–O)	$69 \pm 5$
	$551 \pm 1$ (Co–O)	$51 \pm 5$	$683 \pm 1$ (Fe–O)	$51 \pm 5$
0.2	$466 \pm 1$ (Fe–O)	$53 \pm 5$	$607 \pm 1$ (Co–O)	$52 \pm 5$
	$503 \pm 1$ (Zn–O)	$44 \pm 5$	$642 \pm 1$ (Zn–O)	$68 \pm 5$
	$554 \pm 1$ (Co–O)	$69 \pm 5$	$686 \pm 1$ (Fe–O)	$44 \pm 5$
0.3	$467 \pm 1$ (Fe–O)	$52 \pm 5$	$610 \pm 1$ (Co–O)	$56 \pm 5$
	$505 \pm 1$ (Zn–O)	$37 \pm 5$	$644 \pm 1$ (Zn–O)	$62 \pm 5$
	$555 \pm 1$ (Co–O)	$68 \pm 5$	$687 \pm 1$ (Fe–O)	$41 \pm 5$
0.4	$468 \pm 1$ (Fe–O)	$51 \pm 5$	$608 \pm 1$ (Co–O)	$45 \pm 5$
	$503 \pm 1$ (Zn–O)	$61 \pm 5$	$643 \pm 1$ (Zn–O)	$55 \pm 5$
	$558 \pm 1$ (Co–O)	$69 \pm 5$	$686 \pm 1$ (Fe–O)	$48 \pm 5$
0.5	$465 \pm 1$ (Fe–O)	$53 \pm 5$	$604 \pm 1$ (Co–O)	$45 \pm 5$
	$504 \pm 1$ (Zn–O)	$64 \pm 5$	$639 \pm 1$ (Zn–O)	$64 \pm 5$
	$554 \pm 1$ (Co–O)	$66 \pm 5$	$683 \pm 1$ (Fe–O)	$46 \pm 5$
0.6	$465 \pm 1$ (Fe–O)	$52 \pm 5$	$602 \pm 1$ (Co–O)	$53 \pm 5$
	$503 \pm 1$ (Zn–O)	$59 \pm 5$	$638 \pm 1$ (Zn–O)	$64 \pm 5$
	$547 \pm 1$ (Co–O)	$67 \pm 5$	$682 \pm 1$ (Fe–O)	$49 \pm 5$
0.7	$468 \pm 1$ (Fe–O)	$45 \pm 5$	$605 \pm 1$ (Co–O)	$47 \pm 5$
	$505 \pm 1$ (Zn–O)	$68 \pm 5$	$642 \pm 1$ (Zn–O)	$56 \pm 5$
	$552 \pm 1$ (Co–O)	$45 \pm 5$	$684 \pm 1$ (Fe–O)	$48 \pm 5$
0.8	$468 \pm 1$ (Fe–O)	$47 \pm 5$	$603 \pm 1$ (Co–O)	$42 \pm 5$
	$505 \pm 1$ (Zn–O)	$68 \pm 5$	$640 \pm 1$ (Zn–O)	$67 \pm 5$
	$550 \pm 1$ (Co–O)	$63 \pm 5$	$682 \pm 1$ (Fe–O)	$48 \pm 5$
0.9	$467 \pm 1$ (Fe–O)	$46 \pm 5$	$602 \pm 1$ (Co–O)	$44 \pm 5$
	$504 \pm 1$ (Zn–O)	$65 \pm 5$	$639 \pm 1$ (Zn–O)	$57 \pm 5$
	$552 \pm 1$ (Co–O)	$62 \pm 5$	$682 \pm 1$ (Fe–O)	$61 \pm 5$

The deconvolution of the Raman spectra, as shown for selected spectra in Figure 6, reveal that for low Zn content, the Zn ions substitute the  $\text{Co}^{2+}$  ions in the tetrahedral sites, as indicated by the decrease in the intensity of the peak located at about  $610\text{ cm}^{-1}$ , associated with the  $A_{1g}$  mode of the  $\text{CoO}_4$  units. As the Zn content increases for  $x > 0.4$ , the contribution from the Zn ions in the octahedral sites at about  $510\text{ cm}^{-1}$  increases. The changes in the intensities of the Raman modes attributed to the Fe ions in the tetrahedral sites ( $\sim 680\text{ cm}^{-1}$ ) and octahedral sites ( $\sim 470\text{ cm}^{-1}$ ) indicate changes in the inversion degree with the Co substitution by Zn.

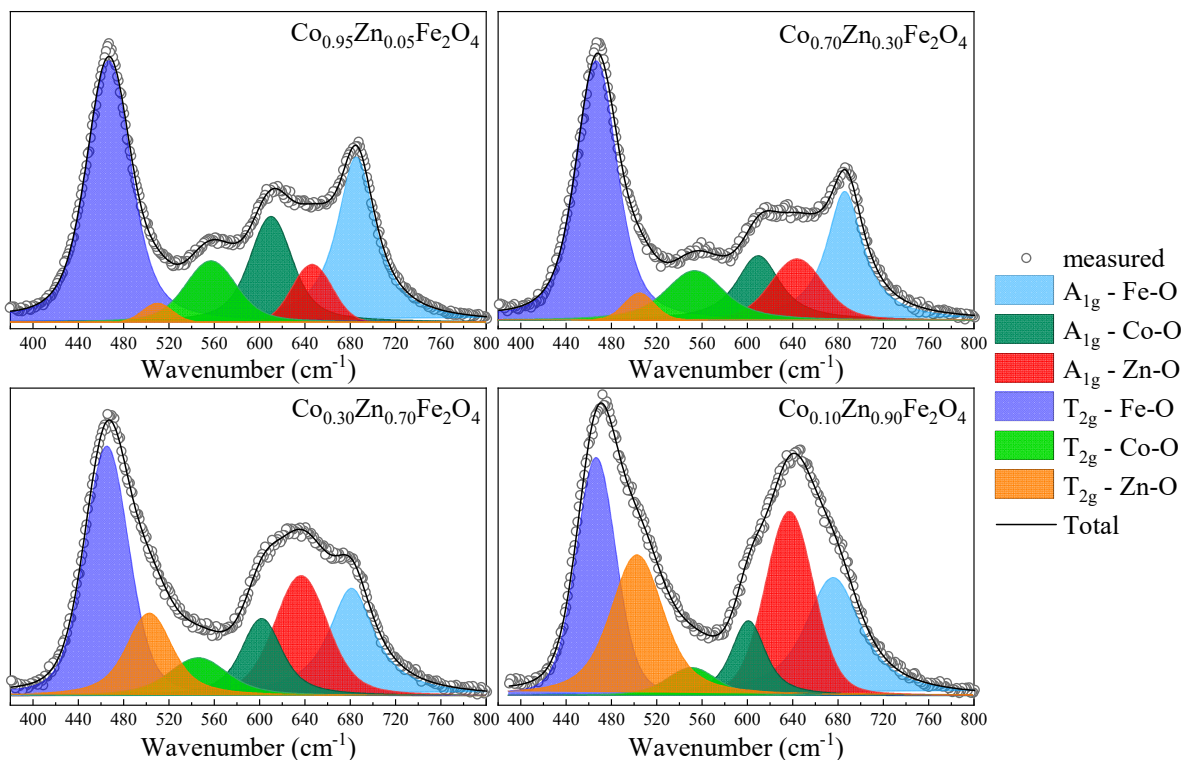


Figure 6. Fitting results for Raman spectra of  $\text{Co}_{1-x}\text{Zn}_x\text{Fe}_2\text{O}_4$  nanoparticles.

### 3.3. Magnetic Measurements

The saturation magnetization,  $M_s$ , at 4 K of  $\text{Co}_{1-x}\text{Zn}_x\text{Fe}_2\text{O}_4$  nanoparticles was determined from magnetic measurements in fields up to 10 T (Figure 7) using the approach to saturation law:

$$M = M_s \left( 1 - \frac{a}{H} \right) + \chi_0 H$$

where  $a$  is the coefficient of magnetic hardness and  $\chi_0$  is the Pauli type contribution.

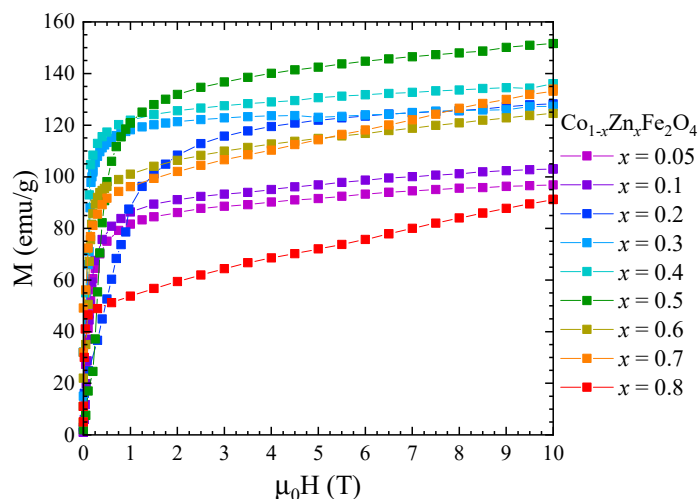
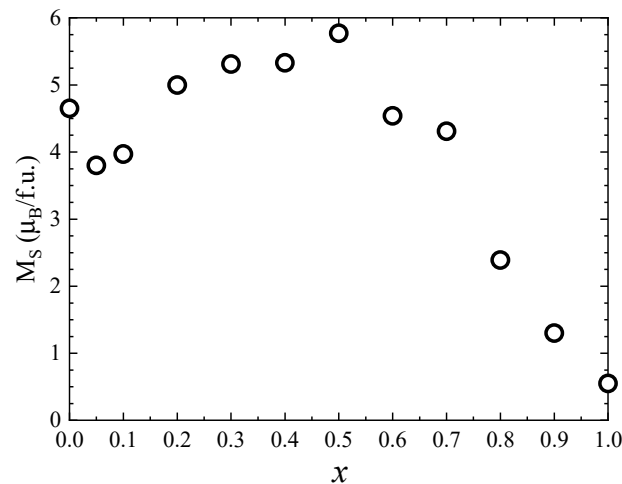


Figure 7. Magnetization isotherms of  $\text{Co}_{1-x}\text{Zn}_x\text{Fe}_2\text{O}_4$  nanoparticles recorded at 4 K.

One can see that the saturation magnetization increases at the beginning when Zn concentration increases with a maximum at  $x = 0.5$ , followed by a strong decrease in the higher Zn content—Figure 8. Previous studies reported a maximum value of the saturation magnetization for  $x = 0.2$  [27] and  $x = 0.4$  [26,28]. The fact that in our case the

maximum saturation magnetization of about  $5.8 \mu_B$  was obtained at higher Zn content can be explained by the high quality and crystallinity of our samples. The initial increase in saturation magnetization with Zn doping level is attributed to the preferential substitution of  $\text{Co}^{2+}$  by nonmagnetic  $\text{Zn}^{2+}$  ions in the tetrahedral sites, in agreement with the Raman data. For  $x \geq 0.5$ , the saturation magnetization decreases, which can be explained by the substitution of Co ions in the octahedral coordination, as indicated by the Raman spectra. The fact that there is no linear dependence of the saturation magnetization with the Zn content for either  $x < 0.5$  or  $x > 0.5$  is consequence of the changes in inversion degree with the concentration.



**Figure 8.** Saturation magnetization of  $\text{Co}_{1-x}\text{Zn}_x\text{Fe}_2\text{O}_4$  nanoparticles.

The magnetic properties of  $\text{Co}_{1-x}\text{Zn}_x\text{Fe}_2\text{O}_4$  nanoparticles at room temperature were also investigated by recording the hysteresis loops between  $-4$  T and  $4$  T (Figure 9). The coercive field has a maximum value of  $0.05$  T for  $x = 0.1$  and decreases with the Zn content for  $x > 0.1$ . The magnetization values at  $300$  K in  $4$  T (Figure 10) show a similar behavior to that of the spontaneous magnetization at  $4$  K.

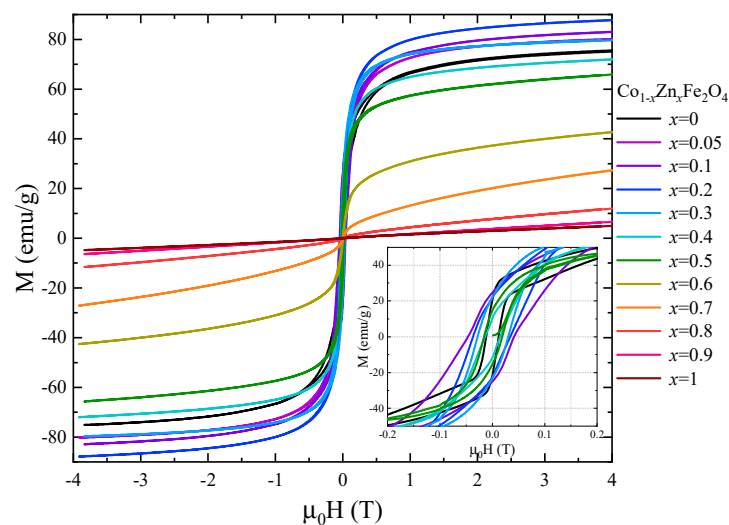


**Figure 9.** Hysteresis loops recorded at room temperature for  $\text{Co}_{1-x}\text{Zn}_x\text{Fe}_2\text{O}_4$  nanoparticles.

The magnetically induced heating capabilities of five samples were investigated in water at one certain concentration of  $1 \text{ mg}_{\text{MNPs}}/\text{mL}$ . The Box–Lucas function was employed to fit the heating curves and the resulting parameters were used to evaluate the specific absorption rate (SAR) in watts per unit mass of MNPs ( $\text{W}/\text{g}_{\text{MNPs}}$ ). The SAR values were

plotted as a function of the amplitude ( $H$ ) of the applied AMF, ranging from 10 kA/m to 60 kA/m (step of 10 kA/m) at a fixed frequency of 355 kHz. The contribution from pure water at each  $H$  was measured and subtracted as the background. Figure 11 summarizes the obtained mean SAR values for the analyzed ferrite particles. The Co ferrites particles without Zn content present low SAR values compared with other studies [47–49]. At the  $H$  of 10 kA/m the SAR is 26 W/g<sub>MNPs</sub>, which increases with the increasing  $H$ , reaching a value of 113 W/g<sub>MNPs</sub> for the highest  $H$  of 60 kA/m used in the study. A Zn doping of 5% and 10% do not significantly influence the heating performances of Co ferrite particles, specifically for  $H$  between 10 and 40 kA/m. A clear increase in SAR values with Zn doping is observed only for the  $H$  of 50 and 60 kA/m. Excepting the field  $H = 10$  kA/m, for the rest values of  $H$  (20–60 kA/m), the SAR values increase considerably for Co ferrite bearing a Zn doping of 20%. A SAR of 88 and 112 W/g<sub>MNPs</sub> is recorded at 20 and 30 kA/m, respectively, which is double that of the previous three samples. Starting with 40 kA/m, the SAR increment is faster, going up to 540 W/g<sub>MNPs</sub> for the highest  $H$  of 60 kA/m. The SAR evolution with  $H$  is typical of a hard sample [47]. It is worth mentioning that, for each  $H$  value, the SAR increased as the Zn doping level was increased. This behavior can be explained by considering the similar dependence of saturation magnetization on the Zn content [50].

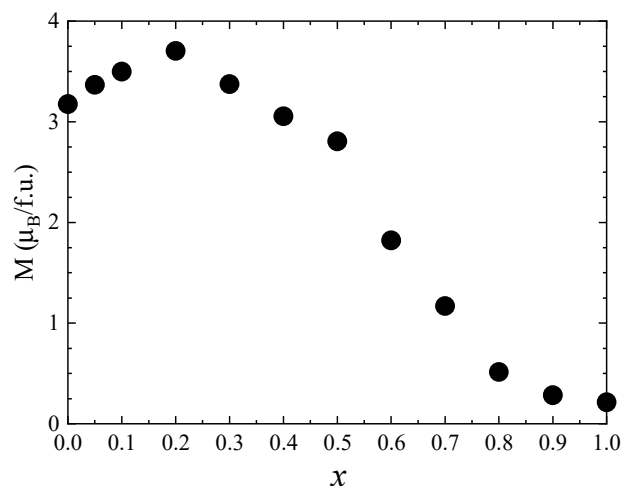


**Figure 10.** The magnetization values in 4 T of  $\text{Co}_{1-x}\text{Zn}_x\text{Fe}_2\text{O}_4$  nanoparticles at 300 K.

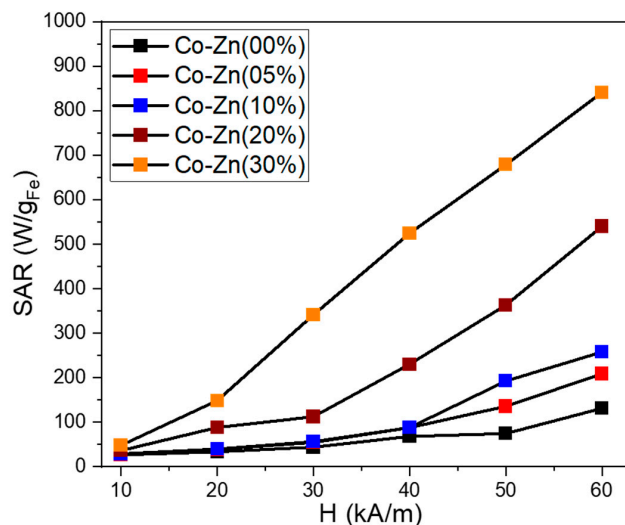


**Figure 11.** Specific absorption rate (SAR) dependence on the magnetic field amplitude ( $H$ ) for the five ferrite samples dispersed in water at a concentration of 1 mg<sub>MNPs</sub>/mL.

The magnetic characterization revealed that by further increasing the Zn content to 30%, both the  $M_s$  and  $H_c$  decreased. However, these particles exhibit the largest SAR values among all five samples. With respect to the previous sample (20% Zn content), the SAR values are enhanced by a factor that increase from 1.3 to 3 as the H is swept from 10 to 60 kA/m. It can be observed that the SAR values increase linearly from 148 to 840 W/g<sub>MNPs</sub> as the H is increased from 20 to 60 kA/m. This peculiar dependence of SAR with the applied H is in accordance with the evolution of magnetization that does not saturate and exhibits a slow positive slope as the external static magnetic field is increased. Due to its very good heating capabilities, this sample represents a good candidate for future in vitro magnetic hyperthermia experiments.

#### 4. Conclusions

Highly crystalline  $\text{Co}_{1-x}\text{Zn}_x\text{Fe}_2\text{O}_4$  nanoparticles ( $0 \leq x \leq 1$ ), with average sizes between 30 nm and 40 nm, have been synthesized via a green sol–gel combustion method, as shown by XRD and TEM structural investigations. Elemental analysis by EDS confirmed the presence of Co, Fe, Zn, and O elements in all studied samples. Raman spectroscopy was employed in analyzing the cation distribution, since the Raman modes corresponding to the Fe, Zn, and Co ions located in the tetrahedral and octahedral sites are well separated in the region between  $380 \text{ cm}^{-1}$  and  $800 \text{ cm}^{-1}$ . The deconvolution of the spectra indicates that for low Zn content ( $x < 0.4$ ), the Zn ions preferentially substitute the  $\text{Co}^{2+}$  ions in the tetrahedral sites. Additionally, the changes in the intensities of the Raman modes attributed to the Fe ions in the tetrahedral sites and octahedral sites suggest changes in the inversion degree with the Co substitution by Zn. The magnetic properties of the investigated nanoparticles reflect the structural changes. Due to their high crystallinity, the nanoparticles show high values of the magnetization, which increases with the Zn content for  $x < 0.5$ , which can be explained by the substitution of Co ions in the tetrahedral sites. For higher Zn concentration, as the Zn ions replace Co in the octahedral sites, the total magnetization of the  $\text{Co}_{1-x}\text{Zn}_x\text{Fe}_2\text{O}_4$  nanoparticles decreases.

The increase in the Zn doping level led to an increase in the heating performances of Co ferrite. With respect to the undoped sample, an SAR enhancement by a factor between 4.5 and 9 over the H range between 20 and 60 kA/m was detected for 30% Zn content.

In the future, we propose to do in vitro hyperthermia experiments and to cover these nanoparticles with a  $\text{BaTiO}_3$  shell in order to test the possibility of controlling the shell electric polarization with the magnetic field while keeping in mind possible applications in cancer treatment.

**Supplementary Materials:** The following are available online at <https://www.mdpi.com/article/10.3390/nano13010189/s1>, the details of magnetic measurements and specific absorption rate (SAR) calculations are provided in the supplementary materials. Reference [51] are cited in the supplementary materials.

**Author Contributions:** Conceptualization, R.T., R.D. and E.B.; investigation, A.S., R.B., G.S., R.D., R.H., L.B.-T., F.N. and C.I.; resources, R.B., A.S. and R.T.; formal analysis, A.S., R.B., G.S., R.D., R.H., L.B.-T., F.N. and C.I.; writing—original draft preparation, A.S., R.B., C.I., R.T. and R.D.; writing—review and editing R.D. and R.T.; visualization, R.D. and R.T.; supervision, R.D., R.T. and E.B.; project administration, R.T. and E.B.; funding acquisition, E.B. and R.T. All authors have read and agreed to the published version of the manuscript.

**Funding:** This research received no external funding.

**Data Availability Statement:** Not applicable.

**Conflicts of Interest:** The authors declare no conflict of interest.

## References

1. Ibrahim, K.; Saeed, K. Khan Idrees Nanoparticles: Properties, applications and toxicities. *Arab. J. Chem.* **2019**, *12*, 908–931. [[CrossRef](#)]
2. Jeevanandam, J.; Barhoum, A.; Chan, Y.S.; Dufresne, A.; Danquah, M.K. Review on nanoparticles and nanostructured materials: History, sources, toxicity and regulations. *Beilstein J. Nanotechnol.* **2018**, *9*, 1050–1074. [[CrossRef](#)] [[PubMed](#)]
3. Sagayaraj, R.; Aravazhi, S.; Chandrasekaran, G. Review on structural and magnetic properties of (Co–Zn) ferrite nanoparticles. *Int. Nano Lett.* **2021**, *11*, 307–319. [[CrossRef](#)]
4. Thakur, P.; Chahar, D.; Taneja, S.; Bhalla, N.; Thakur, A. A review on MnZn ferrites: Synthesis, characterization and applications. *Ceram. Int.* **2020**, *46*, 15740–15763. [[CrossRef](#)] [[PubMed](#)]
5. Balanov, V.A.; Kiseleva, A.P.; Krivoschapkina, E.F.; Kashtanov, E.A.; Gimaev, R.R.; Zverev, V.I.; Krivoschapkin, P.V. Synthesis of  $(\text{Mn}_{1-x}\text{Zn}_x)\text{Fe}_2\text{O}_4$  nanoparticles for magnetocaloric applications. *J. Sol.-Gel. Sci. Technol.* **2020**, *95*, 795–800. [[CrossRef](#)]
6. Krishna, V.D.; Wu, K.; Perez, A.M.; Wang, J.P. Giant magnetoresistance-based biosensor for detection of influenza A virus. *Front. Microbiol.* **2016**, *7*, 400. [[CrossRef](#)] [[PubMed](#)]
7. Srinivasan, Y.S.; Kishore, M.; Paknikar, K.M.; Bodas, D.; Gajbhiye, V. Applications of cobalt ferrite nanoparticles in biomedical nanotechnology. *Nanomedicine* **2018**, *13*, 10. [[CrossRef](#)]
8. Kazemi, M.; Ghobadi, M.; Mirzaie, A. Cobalt ferrite nanoparticles ( $\text{CoFe}_2\text{O}_4$  MNPs) as catalyst and support: Magnetically recoverable nanocatalysts in organic synthesis. *Nanotechnol. Rev.* **2018**, *7*, 43–68. [[CrossRef](#)]
9. Nayeem, F.; Parveez, A.; Chaudhuri, A.; Sinha, R.; Khader, S.A. Effect of Zn<sup>2+</sup> doping on structural, dielectric and electrical properties of cobalt ferrite prepared by auto combustion method. *Mater. Today Proc.* **2017**, *4*, 12138–12143. [[CrossRef](#)]
10. Xi, G.; Xi, Y. Effects on magnetic properties of different metal ions substitution cobalt ferrite synthesis by sol-gel auto-combustion route using used batteries. *Mater. Lett.* **2016**, *164*, 444–448. [[CrossRef](#)]
11. Iacovita, C.; Florea, A.; Scorus, L.; Pall, E.; Dudric, R.; Moldovan, A.I.; Stiufiuc, R.; Tetean, R.; Lucaciu, C.M. Hyperthermia, Cytotoxicity, and Cellular Uptake Properties of Manganese and Zinc Ferrite Magnetic Nanoparticles Synthesized by a Polyol-Mediated Process. *Nanomaterials* **2019**, *9*, 1489. [[CrossRef](#)] [[PubMed](#)]
12. Tatarchuk, T.R.; Paliychuk, N.D.; Bououdina, M.; Al-Najar, B.; Pacia, M.; Macyk, W.; Shyichuk, A. Effect of cobalt substitution on structural, elastic, magnetic and optical properties of zinc ferrite nanoparticles. *J. Alloys Comp.* **2018**, *731*, 1256–1266. [[CrossRef](#)]
13. Naik, M.M.; Naik, H.B.; Nagaraju, G.; Vinuth, M.; Vinu, K.; Viswanath, R. Green synthesis of zinc doped cobalt ferrite nanoparticles: Structural, optical, photocatalytic and antibacterial studies. *Nano-Struct. Nano-Objects* **2019**, *19*, 100322. [[CrossRef](#)]
14. Chakradhary, V.K.; Ansari, A.; Akhtar, M.J. Design, synthesis and testing of high coercivity cobalt doped nickel ferrite nanoparticles for magnetic applications. *J. Magn. Magn. Mater.* **2019**, *469*, 674–680. [[CrossRef](#)]
15. Dippong, T.; Levei, E.A.; Cadar, O. Recent Advances in Synthesis and Applications of  $\text{MFe}_2\text{O}_4$  (M = Co, Cu, Mn, Ni, Zn) Nanoparticles. *Nanomaterials* **2021**, *11*, 1560. [[CrossRef](#)]
16. Kaur, H.; Singh, A.; Kumar, A.; Ahlawat, D.S. Structural, thermal and magnetic investigations of cobalt ferrite doped with  $\text{Zn}^{2+}$  and  $\text{Cd}^{2+}$  synthesized by auto combustion method. *J. Magn. Magn. Mater.* **2019**, *474*, 505–511. [[CrossRef](#)]
17. Xiong, Q.Q.; Tu, J.P.; Shi, S.J.; Liu, X.Y.; Wang, X.L.; Gu, C.D. Ascorbic acid-assisted synthesis of cobalt ferrite ( $\text{CoFe}_2\text{O}_4$ ) hierarchical flower-like microspheres with enhanced lithium storage properties. *J. Power Sources* **2014**, *256*, 153–159. [[CrossRef](#)]
18. Torkian, S.; Ghasemi, A.; Razavi, R.S. Cation distribution and magnetic analysis of wideband microwave absorptive  $\text{Co}_x\text{Ni}_{1-x}\text{Fe}_2\text{O}_4$  ferrites. *Ceram. Int.* **2017**, *43*, 6987–6995. [[CrossRef](#)]
19. Mahala, C.; Sharma, M.D.; Basu, M. 2D nanostructures of  $\text{CoFe}_2\text{O}_4$  and  $\text{NiFe}_2\text{O}_4$ : Efficient oxygen evolution catalyst. *Electrochim. Acta* **2018**, *273*, 462–473. [[CrossRef](#)]
20. Manikandan, A.; Sridhar, R.; Arul, S.A.; Ramakrishna, S. A simple aloe vera plant-extracted microwave and conventional combustion synthesis: Morphological, optical, magnetic and catalytic properties of  $\text{CoFe}_2\text{O}_4$  nanostructures. *J. Molec. Struct.* **2014**, *1076*, 188–200. [[CrossRef](#)]
21. Li, X.; Sun, Y.; Zong, Y.; Wei, Y.; Liu, X.; Li, X.; Peng, Y.; Zheng, X. Size-effect induced cation redistribution on the magnetic properties of well-dispersed  $\text{CoFe}_2\text{O}_4$  nanocrystals. *J. Alloy Comp.* **2020**, *841*, 155710. [[CrossRef](#)]
22. Nlebedim, I.C.; Snyder, J.E.; Moses, A.J.; Jiles, D.C. Dependence of the magnetic and magnetoelastic properties of cobalt ferrite on processing parameters. *J. Magn. Magn. Mater.* **2010**, *322*, 3938–3942. [[CrossRef](#)]
23. Muhammad, A.; Sato-Turtelli, R.; Kriegisch, M.; Grössinger, R.; Kubel, F.; Konegger, T. Large enhancement of magnetostriction due to compaction hydrostatic pressure and magnetic annealing in  $\text{CoFe}_2\text{O}_4$ . *J. App. Phys.* **2012**, *111*, 013918. [[CrossRef](#)]
24. Köseoğlu, Y.; Alan, F.; Tan, M.; Yilgin, R.; Öztürk, M. Low temperature hydrothermal synthesis and characterization of Mn doped cobalt ferrite nanoparticles. *Ceram. Int.* **2012**, *38*, 3625–3634. [[CrossRef](#)]
25. Dippong, T.; Levei, E.A.; Cadar, O. Investigation of Structural, Morphological and magnetic properties of  $\text{MFe}_2\text{O}_4$  (M = Co, Ni, Zn, Cu, Mn) obtained by thermal decomposition. *Int. J. Mol. Sci.* **2022**, *23*, 8483. [[CrossRef](#)]
26. Wang, L.; Li, F.-S. Structural and magnetic properties of  $\text{Co}_{1-x}\text{Zn}_x\text{Fe}_2\text{O}_4$  nanoparticles. *Chin. Phys. B* **2008**, *17*, 1858. [[CrossRef](#)]
27. Slatineanu, T.; Iordan, A.R.; Oancea, V.; Palamaru, M.N.; Dumitru, I.; Constantin, C.P.; Caltun, O.F. Magnetic and dielectric properties of Co–Zn ferrite. *Mater. Sci. Eng. B* **2013**, *178*, 1040–1047. [[CrossRef](#)]
28. Atif, M.; Asghar, M.W.; Nadeem, M.; Khalid, W.; Ali, Z.; Badshah, S. Synthesis and investigation of structural, magnetic and dielectric properties of zinc substituted cobalt ferrites. *J. Phys. Chem. Solids* **2018**, *123*, 36–42. [[CrossRef](#)]

29. Tanaka, K.; Makita, M.; Shimizugawa, Y.; Hirao, K.; Soga, N. Structure and high magnetization of rapidly quenched zinc ferrite. *J. Phys. Chem. Solids* **1998**, *59*, 1611–1618. [[CrossRef](#)]
30. Bortnic, R.; Szatmari, A.; Souca, G.; Hirian, R.; Dudric, R.; Barbu-Tudoran, L.; Toma, V.; Tetean, R.; Burzo, E. New Insights into the Magnetic Properties of  $\text{CoFe}_2\text{O}_4@ \text{SiO}_2@ \text{Au}$  Magnetoplasmonic Nanoparticles. *Nanomaterials* **2022**, *12*, 942. [[CrossRef](#)]
31. Burzo, E.; Tetean, R. New insights on the Spin Glass Behavior in Ferrites Nanoparticles. *Nanomaterials* **2022**, *12*, 1782. [[CrossRef](#)] [[PubMed](#)]
32. Liu, S.; Tao, D.; Zhang, L. Cellulose scaffold: A green template for the controlling synthesis of magnetic inorganic nanoparticles. *Powder Technol.* **2012**, *217*, 502–509. [[CrossRef](#)]
33. Hermosa, G.C.; Liao, C.S.; Wu, H.S.; Wang, S.F.; Liu, T.Y.; Jeng, K.S.; Lin, S.S.; Chang, C.F.; Sun, A.A. Green Synthesis of Magnetic Ferrites ( $\text{Fe}_3\text{O}_4$ ,  $\text{CoFe}_2\text{O}_4$ , and  $\text{NiFe}_2\text{O}_4$ ) Stabilized by Aloe Vera Extract for Cancer Hyperthermia Activities. *IEEE Trans. Magn.* **2022**, *58*, 5400307. [[CrossRef](#)]
34. Rietveld, H.M. A profile refinement method for nuclear and magnetic structures. *J. Appl. Crystallogr.* **1969**, *2*, 65. [[CrossRef](#)]
35. De Faria, D.L.A.; Venâncio Silva, S.; de Oliveira, M.T. Raman Microspectroscopy of Some Iron Oxides and Oxyhydroxide. *J. Raman Spectrosc.* **1997**, *28*, 873. [[CrossRef](#)]
36. Graves, P.R.; Johnston, C.; Campaniello, J.J. Raman scattering in spinel structure ferrites. *Mater. Res. Bull.* **1988**, *23*, 1651–1660. [[CrossRef](#)]
37. Wang, Z.; Lazor, P.; Saxena, S.K.; O'Neill, H.S.C. High pressure Raman spectroscopy of ferrite  $\text{MgFe}_2\text{O}_4$ . *Mater. Res. Bull.* **2002**, *37*, 1589–1602. [[CrossRef](#)]
38. de Wijs, G.A.; Fang, C.M.; Kresse, G. First-principles calculation of the phonon spectrum of  $\text{MgAl}_2\text{O}_4$  spinel. *Phys. Rev. B* **2002**, *65*, 094305. [[CrossRef](#)]
39. Lazzeri, M.; Thibaudeau, P. Ab initio Raman spectrum of the normal and disordered  $\text{MgAl}_2\text{O}_4$  spinel. *Phys. Rev. B* **2006**, *74*, 140301. [[CrossRef](#)]
40. Chourpa, I.; Douziech-Eyrolles, L.; Ngaboni-Okassa, L.; Fouquenot, J.F.; Cohen-Jonathan, S.; Souce, M.; Marchais, H.; Dubois, P. Molecular composition of iron oxide nanoparticles, precursors for magnetic drug targeting, as characterized by confocal Raman microspectroscopy. *Analyst* **2005**, *130*, 1395–1403. [[CrossRef](#)]
41. Chandramohan, P.; Srinivasan, M.P.; Velmurugan, S.; Narasimhan, S.V. Cation distribution and particle size effect on Raman spectrum of  $\text{CoFe}_2\text{O}_4$ . *J. Solid State Chem.* **2011**, *184*, 89–96. [[CrossRef](#)]
42. Thota, S.; Kashyap, S.C.; Sharma, S.K.; Reddy, V.R. Micro Raman, Mossbauer and magnetic studies of manganese substituted zinc ferrite nanoparticles: Role of Mn. *Phys. Chem. Solid* **2015**, *91*, 136. [[CrossRef](#)]
43. Testa-Anta, M.; Ramos-Docampo, M.A.; Comesaña-Hermo, M.; Rivas-Murias, B.; Salgueiriño, V. Raman spectroscopy to unravel the magnetic properties of iron oxide nanocrystals for bio-related applications. *Nanoscale Adv.* **2019**, *1*, 2086–2103. [[CrossRef](#)]
44. Nekvapil, F.; Bunge, A.; Radu, T.; Cinta Pinzaru, S.; Turcu, R. Raman spectra tell us so much more: Raman features and saturation magnetization for efficient analysis of manganese zinc ferrite nanoparticles. *J. Raman Spectrosc.* **2020**, *51*, 959–968. [[CrossRef](#)]
45. Nekvapil, F.; Bortnic, R.A.; Leoştean, C.; Barbu-Tudoran, L.; Bunge, A. Characterization of the lattice transitions and impurities in manganese and zinc doped ferrite nanoparticles by Raman spectroscopy and x-ray diffraction (XRD). *Anal. Lett.* **2022**, *56*, 42–52. [[CrossRef](#)]
46. Galinetto, P.; Albin, B.; Bini, M.; Mozzati, M. Raman spectroscopy in Zinc Ferrites Nanoparticles. In *Raman Spectroscopy*; IntechOpen: London, UK, 2018. [[CrossRef](#)]
47. Iacovita, C.; Stiuftuc, G.F.; Dudric, R.; Vedeanu, N.; Tetean, R.; Stiuftuc, R.I.; Lucaciu, C.M. Saturation of Specific Absorption Rate for Soft and Hard Spinel Ferrite Nanoparticles Synthesized by Polyol Process. *Magnetochemistry* **2020**, *6*, 23. [[CrossRef](#)]
48. Mameli, V.; Musinu, A.; Ardu, A.; Ennas, G.; Peddis, D.; Niznansky, D.; Sangregorio, C.; Innocenti, C.; Nguyen, T.K.; Cannas, C. Studying the effect of Zn-substitution on the magnetic and hyperthermic properties of cobalt ferrite nanoparticles. *Nanoscale* **2016**, *8*, 10124–10137. [[CrossRef](#)]
49. Sathya, A.; Guardia, P.; Brescia, R.; Silvestri, N.; Pugliese, G.; Nitti, S.; Manna, L.; Pellegrino, T.  $\text{Co}_x\text{Fe}_{3-x}\text{O}_4$  Nanocubes for Theranostic Applications: Effect of Cobalt Content and Particle Size. *Chem. Mater.* **2016**, *28*, 1769–1780. [[CrossRef](#)]
50. Albino, M.; Fantechi, E.; Innocenti, C.; López-Ortega, A.; Bonanni, V.; Campo, G.; Pineider, F.; Gurioli, M.; Arosio, P.; Orlando, T.; et al. Role of  $\text{Zn}^{2+}$  Substitution on the Magnetic, Hyperthermic, and Relaxometric Properties of Cobalt Ferrite Nanoparticles. *J. Phys. Chem. C* **2019**, *123*, 6148–6157. [[CrossRef](#)]
51. Iacovita, C.; Stiuftuc, R.; Radu, T.; Florea, A.; Stiuftuc, G.; Dutu, A.; Mican, S.; Tetean, R.; Lucaciu, C.M. Polyethylene glycol mediated synthesis of cubic iron oxide nanoparticles with high heating power. *Nanoscale Res. Lett.* **2015**, *10*, 1–16. [[CrossRef](#)]

**Disclaimer/Publisher's Note:** The statements, opinions and data contained in all publications are solely those of the individual author(s) and contributor(s) and not of MDPI and/or the editor(s). MDPI and/or the editor(s) disclaim responsibility for any injury to people or property resulting from any ideas, methods, instructions or products referred to in the content.